Subthreshold Electron Transport Properties of Ultrascaled Phase Change Memory

Jie Liu, Xu Xu, and Manjeri P. Anantram

***Abstract*— This letter investigates the subthreshold electron transport properties of ultrascaled phase change material (PCM) GeTe, which is sandwiched by TiN electrodes, by using *ab initio* molecular dynamics, density functional theory, and Green's function. Our purely *ab initio* simulations reproduce the measured current–voltage curve characteristics of crystalline (*c*-) and amorphous (*a*-) PCM. The ON/OFF ratio and the underlying electron transport mechanism are explained. The electron transport properties of ultrascaled *c*-PCM are dominated by metal-induced gap states, and the measured linear and exponential shapes of the subthreshold current–voltage curve of ultrascaled *a*-PCM are a consequence of both the bias window enlarging and the bias-induced change of transmission.**

***Index Terms*— Phase change memory, device scaling, *ab initio* molecular dynamics, density functional theory, Green's function.**

I. Introduction

THE phase change memory is promising to become the mainstream nonvolatile data storage technology, due to its fast speed, low energy consumption, and superb scalability [1]–[11]. The state-of-art PCM scaling experiments have found that the PCM devices still can operate stably with about two orders of magnitude ON/OFF ratio, even when they are scaled to 6 nm [6]. The superb scalability of PCM is particularly useful to enable ultra-dense data storage solutions. Actually, the ultimate scalability of PCM technology largely hinges on nano-scale electron transport properties [1]. However, though the electron transport properties of bulk PCM have been well studied [12]–[17], those of the ultra-scaled PCM nanostructures (sub-10 nm) are still poorly understood. It is important to study them, in order to better understand the underlying device physics and to improve ultra-dense PCM device design. While the equilibrium (bias v=0) electron transport properties have been studied in our previous work [1], here we simulate the electron transport properties of the ultra-scaled a-GeTe and c-GeTe at finite biases.

II. Simulation Model and Algorithm

In this letter, we study binary PCM GeTe, instead of the most popular ternary $Ge_2Sb_2Te_5$, since binary PCM has better scalability [8], [9]. Here, we focus on the sub-threshold bias region, as the threshold switching possibly involves local crystallization, which is much more difficult to model. The ab initio simulations are used to create the models shown in Fig. 1. The c-GeTe model is obtained by relaxing the measured lattice structure [18] using conjugate gradient (CG). The melt-quench AIMD simulations are used to obtain the a-GeTe model. The sandwich models (Fig. 1) are created by relaxing the atoms near the TiN/GeTe interfaces using CG. DFT simulations are used to obtain the Hamiltonian (**H**) and overlap (**S**) matrices, which contain ab initio description of the electronic structure. The AIMD, CG, and DFT simulations are performed using the SIESTA package [19]. The simulations use a single realization of the amorphous structure. Future work that accounts for sample-to-sample variation is an important direction. Further details of simulation algorithms and model validation can be found in our prior work [1], [20], and [21].

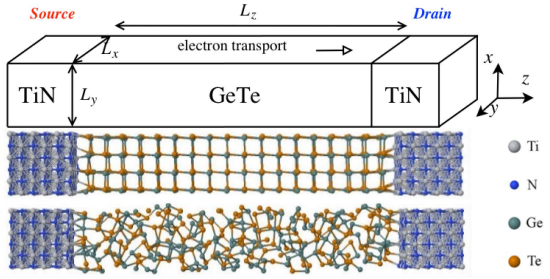


Fig. 1. Atomistic scale electron transport simulation models (L_x=L_y≈1.2 nm, and L_z≈6.0 nm), which are created using ab initio simulations [1].

When a bias v is applied, the current density

$$J_e = (2q_e/\hbar L_x L_y) \int_{-\infty}^{+\infty} d\epsilon T \, (f_S - f_D) \tag{1}$$

is computed using GF, where $\hbar$ is the reduced Planck constant; q_e is the elementary charge; ϵ is the electron energy;

$$T = \mathrm{Tr}\left[\mathbf{\Gamma}_S \mathbf{G}^r \mathbf{\Gamma}_D \mathbf{G}^{r\dagger}\right] \tag{2}$$

is the transmission; $\mathbf{\Gamma}_{S/D}$ is the source/drain broadening matrix;

$$\mathbf{G}^r = (\epsilon \mathbf{S} - \mathbf{H} - \Delta\mathbf{H} - \mathbf{\Sigma}_S - \mathbf{\Sigma}_D)^{-1} \tag{3}$$

is retarded Green's function; $\mathbf{\Sigma}_{S/D}$ is source/drain self energy; $\Delta\mathbf{H}_{\mu\nu} \approx (\phi_\mu + \phi_\nu)\mathbf{S}_{\mu\nu}/2$ is to account for the approximately linear potential variation between source and drain; ϕ_μ is potential at the atom to which the orbital μ belongs;

$$f_{S/D} = (1 + e^{(\epsilon - \epsilon_F \pm v/2)/k_B T_0})^{-1} \tag{4}$$

is the Fermi function of source/drain; ϵ_F is the Fermi level; k_B is the Boltzmann constant; and T_0 is the room temperature.

In Eq. (1-3), the Zener tunneling and the elastic scattering of electrons are naturally included; and the inelastic scattering of

Manuscript received February 4, 2014; revised February 26, 2014 and March 6, 2014; accepted March 10, 2014. Date of publication March 24, 2014; date of current version April 22, 2014. This work was supported by the U.S. National Science Foundation under Grant 1006182. The review of this letter was arranged by Editor L. Selmi.

The authors are with the Department of Electrical Engineering, University of Washington, Seattle, WA 98195 USA (e-mail: liujie@uw.edu).

Color versions of one or more of the figures in this letter are available online at http://ieeexplore.ieee.org.

Digital Object Identifier 10.1109/LED.2014.2311461

0741-3106 © 2014 IEEE. Personal use is permitted, but republication/redistribution requires IEEE permission.
See http://www.ieee.org/publications_standards/publications/rights/index.html for more information.

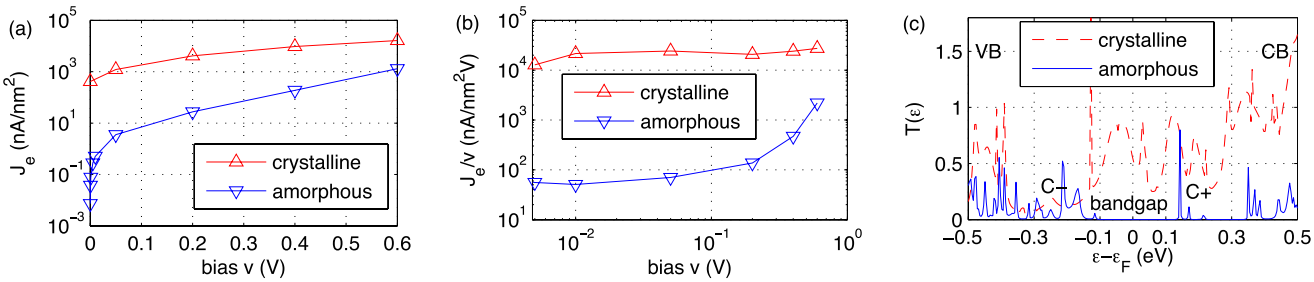


Fig. 2. The current-voltage curve (a), conductance (b), and transmission coefficients when v=0 (c) of ultra-scaled PCM. Here, J_e is current density; v is bias; ε is electron energy; ε_F is Fermi level; T is transmission; C+/C- is intra-bandgap donor/acceptor-like defect states; VB is valence band; and CB is conduction band.

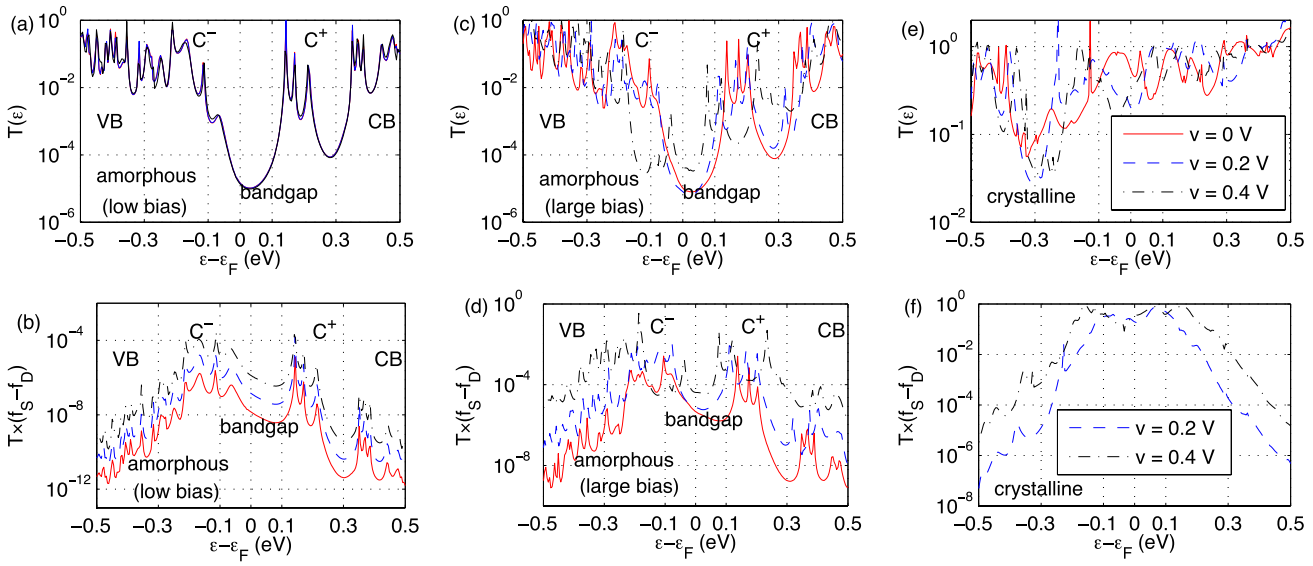


Fig. 3. Bias-dependent energy-resolved electron transport properties of ultra-scaled PCM. (a)–(b): low-bias transport properties of a-GeTe (red solid line, blue dashed line, black dash-dot line mean that the bias is 0.0001 V, 0.001V, and 0.01 V, respectively); (c)–(d): large-bias transport properties of a-GeTe (red solid line, blue dashed line, black dash-dot line mean that the bias is 0.05 V, 0.2 V, 0.4 V, respectively); (e)–(f): transport properties of c-GeTe. Here, $f_{S/D}$ is Fermi function of source/drain; and other symbols are explained in Fig. 2.

electrons is ignored, which is justified since the channel length of our interest here (L_z =6 nm in Fig. 1) is much smaller than the electron mean free path in PCM (10^1 nm [8], [10]).

III. Simulation Results

The ab initio simulations (Fig. 2) reproduce the measured linear (exponential) current-voltage curve shape of the a-GeTe in sub-threshold low (large) bias region [6], [8]. The linear shape of measured c-GeTe current-voltage curve is also reproduced [Fig. 2(b)]. When bias v is about 0.2 V (typical read operation bias), the c-GeTe is about 10^2 times more conductive than the a-GeTe [Fig. 2(b)]. The large conductance contrast establishes an adequate ON/OFF ratio, which is indispensible for ultra-scaled PCM devices to store data. It worth noting that the simulated ON/OFF ratio (about 10^2) agrees well with the measured two orders of magnitude ON/OFF ratio of PCM devices ultra-scaled to the same size [6].

The physical origin of the ON/OFF ratio of the ultra-scaled PCM can be found in the transmission [Fig. 2(c)]. It can be seen that the a-GeTe shows a bandgap near the Fermi level, even when it is ultra-scaled to 6 nm. In contrast, the c-GeTe scaled to the same size does not have any bandgap and the transmission is very large near the Fermi level. To better understand the underlying physics of the results shown in Fig. 2, the bias-dependent and energy-resolved electron transport properties are studied in Fig. 3, where $T\times(f_S\text{-}f_D)$ as a function of ϵ represents the contribution of the electrons with energy ϵ to the total current in units of a constant $2q_e/\hbar L_x L_y$ [Eq. (1)].

In the low bias region (when v is smaller than about 0.05 V), the transmission of a-GeTe is roughly independent of bias [Fig. 3(a)]. The linear shape of the a-GeTe current-voltage curve is merely caused by the energy-independent linear increase of $T\times(f_S\text{-}f_D)$ as the bias increases [Fig. 3(b)]. This is just a manifestation of the bias window enlarging described in the term $f_S\text{-}f_D$, which depends linearly on bias when bias is small.

In the large bias region (when v is larger than about 0.05 V), the transmission of a-GeTe becomes bias-dependent [Fig. 3(c)]. Also, as the bias increases, the dependence of $f_S\text{-}f_D$ on the bias becomes exponential at energies near the intra-gap donor-like and acceptor-like defect states (Eq. (4)). Therefore, the exponential shape of the a-GeTe current-voltage curve is a consequence of both the bias window enlarging and the bias-induced change of transmission [Fig. 3(d)].

By comparing Fig. 3(c) and (d) and Fig. 3(e) and (f), it can be seen more clearly that, when the bias v is applied, the small (large) transmission of the a-GeTe (c-GeTe) leads to small (large) $T\times(f_S\text{-}f_D)$ near the Fermi level. Consequently, the electrical conduction of the ultra-scaled a-GeTe is mainly due to the electron transport via intra-gap donor-like and acceptor-like defect states [Fig. 3(a)–(d)]. In sharp contrast, since the

c-GeTe ultra-scaled to the same size has no bandgap, the electrical conduction in c-GeTe is dominated by electron transport near the Fermi level [Fig. 3(e) and (f)]. This distinctive fundamental transport mechanism difference is the physical origin of the two orders of magnitude ON/OFF ratio shown in Fig. 2.

Since the bulk a-GeTe (c-GeTe) is a semiconductor with about 0.8 (0.2) eV bandgap [8], it is interesting to understand why the bandgap of a-GeTe (c-GeTe) exists (vanishes) in the ultra-scaled nanostructures. This difference is caused by the different behaviors of the metal induced gap states (MIGS) in these two phases. It is well know that the MIGS penetrate deeper into semiconductors with smaller bandgap. As a result, while the MIGS exist only in the a-GeTe regions very close to the metal electrodes, they penetrate all the way through the c-GeTe, leading to large density of states and transmission near the Fermi level [1].

Besides vanishing of c-GeTe bandgap, aggressive scaling also changes the underlying electron transport mechanism from inelastic/diffusive to largely elastic. In bulk PCM devices, where the channel length is much larger than the electron mean free path (measured to be about 10^1 nm [8], [10]) of PCM, the electrons can encounter multiple inelastic scattering events when they are transported from source to drain. This is not only essential for the Poole-Frenkel model (inelastic scattering helps electrons hop over the potential barriers), but also indispensable for the Ohm's law (multiple phase incoherent scattering events is the underlying mechanism of diffusive electron transport).

When PCM devices are ultra-scaled (say, to sub-10 nm), the channel length becomes comparable to (or smaller than) the electron mean free path. As a result, the inelastic scattering probability is significantly reduced, and the transport becomes largely elastic. It has been estimated that when PCM devices are ultra-scaled to 6 nm, less than 4% of the electron energy is lost via inelastic scattering [20], indicating that the electron transport is largely elastic in the ultra-scaled PCM devices.

Interestingly, though the experimentally measured electron transport properties of the ultra-scaled PCM resemble those of bulk PCM, their underlying physical mechanisms are different. While the linear (exponential) shape of the bulk a-PCM current-voltage curve in sub-threshold small (large) bias region is caused by the inelastic scattering of trapped electrons (Poole-Frenkel law) [12]–[17], the similar shape of the ultra-scaled a-PCM [Fig. 2(a) and (b)] is caused by the elastic electron transport via intra-bandgap donor-like and acceptor-like defect states [Fig. 3(a)–(d)]. While the linear shape of the bulk c-PCM current-voltage curve stems from diffusive electron transport due to various inelastic scattering processes (Ohm's law), the similar shape of ultra-scaled c-PCM [Fig. 2(a) and (b)] stems from the elastic electron transport near the Fermi level [Fig. 3(e) and (f)]. Though disguised by phenomenological resemblance, these differences of underlying physics between ultra-scaled PCM and bulk PCM should be appreciated, in order to understand the device physics and to improve the design of ultra-scaled PCM devices.

IV. Conclusion

The sub-threshold electron transport properties of the ultra-scaled PCM GeTe under non-zero bias are investigated using ab initio simulations. The measured characteristics of current-voltage curves of the ultra-scaled a-GeTe and c-GeTe are reproduced and explained. It is found that the low-bias linear region of the a-GeTe current-voltage curve originates from the bias window enlarging; the large-bias exponential region of the a-GeTe current-voltage curve is due to both the bias window enlarging and the bias-induced change of the transmission; and the linear shape of c-GeTe current-voltage curve is due to the elastic electron transport near the Fermi level. It is pointed out that the underlying electron transport mechanisms of ultra-scaled PCM devices are totally different from its bulk counterpart. The difference is relevant to better design and further improve deeply scaled PCM devices.

References

[1] J. Liu and M. P. Anantram, "Low-bias electron transport properties of germanium telluride ultrathin films," *J. Appl. Phys.*, vol. 113, no. 6, p. 063711, 2013.

[2] D. Loke, T. H. Lee, W. J. Wang *et al.*, "Breaking the speed limits of phase-change memory," *Science*, vol. 336, no. 6088, pp. 1566–1569, 2012.

[3] F. Xiong, A. Liao, D. Estrada *et al.*, "Low-power switching of phase-change materials with carbon nanotube electrodes," *Science*, vol. 332, no. 6029, pp. 568–570, 2011.

[4] J. Liu, B. Yu, and M. P. Anantram, "Scaling analysis of nanowire phase change memory," *IEEE Electron Device Lett.*, vol. 32, no. 10, pp. 1340–1342, Oct. 2011.

[5] J. Liu, B. Yu, and M. P. Anantram, "Isotropic and anisotropic scaling analysis of nanowire phase change memory," in *Proc. 11th IEEE Conf. Nanotechnol.*, Portland, OR, USA, Aug. 2011, pp. 1343–1347.

[6] S. Kim, B. J. Bae, Y. Zhang *et al.*, "One-dimensional thickness scaling study of phase change material using a pseudo 3-terminal device," *IEEE Trans. Electron Device*, vol. 58, no. 5, pp. 1483–1489, May 2011.

[7] H.-S. P. Wong, S. Raoux, S. Kim *et al.*, "Phase change memory," *Proc. IEEE*, vol. 98, no. 12, pp. 2201–2227, Jun. 2010.

[8] S. Raoux and M. Wuttig, *Phase Change Materials Science and Applications*. New York, NY, USA: Springer-Verlag, 2009.

[9] S. Raoux, J. L. Jordan-Sweet, A. J. Kellock *et al.*, "Crystallization properties of ultrathin phase change films," *J. Appl. Phys.*, vol. 103, no. 11, p. 114310, 2008.

[10] D. Yu, S. Brittman, and J. S. Lee, "Minimum voltage for threshold switching in nanoscale phase change memory," *Nano. Lett.*, vol. 8, no. 10, pp. 3429–3433, 2008.

[11] S. Kim and H.-S. P. Wong, "Analysis of temperature in phase change memory scaling," *IEEE Electron Device Lett.*, vol. 28, no. 8, pp. 697–699, Aug. 2007.

[12] D. Ielmini, "Threshold switching mechanism by high-field energy gain in the hopping transport of chalcogenide glasses," *Phys. Rev. B*, vol. 78, no. 3, pp. 035308-1–035308-3, 2008.

[13] D. Ielmini and Y. Zhang, "Analytical model for sub-threshold conduction and threshold switching in chalcogenide-based memory devices," *J. Appl. Phys.*, vol. 102, no. 5, pp. 054517-1–054517-13, 2007.

[14] D. Ielmini and Y. Zhang, "Evidence for trap-limited transport in the subthreshold conduction regime of chalcogenide glasses," *Appl. Phys. Lett.*, vol. 90, no. 19, pp. 192102-1–192102-3, 2007.

[15] A. Redaelli, A. Pirovano, F. Pellizzer *et al.*, "Electronic switching effect and phase-change transition in chalcogenide materials," *IEEE Electron Device Lett.*, vol. 25, no. 10, pp. 684–686, Oct. 2004.

[16] E. Piccinini, A. Cappelli, F. Buscemi *et al.*, "Hot-carrier trap-limited transport in switching chalcogenides," *J. Appl. Phys.*, vol. 112, no. 8, p. 083722, 2012.

[17] G. B. Beneventi, L. Guarino, M. Ferro *et al.*, "Three-dimensional Poole-Frenkel analytical model for carrier transport in amorphous chalcogenides," *J. Appl. Phys.*, vol. 113, no. 4, pp. 044506-1–044506-10, 2013.

[18] T. Chattopadhyay, J. X. Boucherle, and H. G. Schnering, "Neutron diffraction study on the structural phase transition in GeTe," *J. Phys. C*, vol. 20, no. 10, p. 1431, 1987.

[19] J. M. Soler, E. Artacho, J. D. Gale *et al.*, "The SIESTA method for *abinitio* order-*N* materials simulation," *J. Phys., Cond. Mat.*, vol. 14, no. 11, pp. 2745–2779, 2002.

[20] J. Liu, "Multiscale simulation of phase change memory," Ph.D. dissertation, Dept. Electr. Eng., Univ. Washington, Seattle, WA, USA, 2013.

[21] J. Liu, X. Xu, L. Brush *et al.*, "A multi-scale analysis of the crystallization of amorphous germanium telluride using *abinitio* simulations and classical crystallization theory," *J. Appl. Phys.*, vol. 115, no. 2, pp. 023513-1–023513-7, 2014.